ACS NANO

www.acsnano.org

ARTICLE

Poly(ionic liquid) Nanovesicle-Templated Carbon Nanocapsules Functionalized with Uniform Iron Nitride Nanoparticles as Catalytic Sulfur Host for Li–S Batteries

Dongjiu Xie, Yaolin Xu, Yonglei Wang, Xuefeng Pan, Eneli Härk, Zdravko Kochovski, Alberto Eljarrat, Johannes Müller, Christoph T. Koch, Jiayin Yuan,* and Yan Lu*

Cite This: *ACS Nano* 2022, 16, 10554–10565

Read Online

ACCESS | Metrics & More | Article Recommendations | Supporting Information

ABSTRACT: Poly(ionic liquid)s (PIL) are common precursors for heteroatom-doped carbon materials. Despite a relatively higher carbonization yield, the PIL-to-carbon conversion process faces challenges in preserving morphological and structural motifs on the nanoscale. Assisted by a thin polydopamine coating route and ion exchange, imidazolium-based PIL nanovesicles were successfully applied in morphology-maintaining carbonization to prepare carbon composite nanocapsules. Extending this strategy further to their composites, we demonstrate the synthesis of carbon composite nanocapsules functionalized with iron nitride nanoparticles of an ultrafine, uniform size of 3–5 nm (termed "Fe_xN@C"). Due to its unique nanostructure, the sulfur-loaded Fe_xN@C electrode was tested to efficiently mitigate the notorious shuttle effect of lithium polysulfides (LiPSs) in Li–S batteries. The cavity of the carbon nanocapsules was spotted to better the loading content of sulfur. The well-dispersed iron nitride nanoparticles effectively catalyze the conversion of LiPSs to Li_2S, owing to their high electronic conductivity and strong binding power to LiPSs. Benefiting from this well-crafted composite nanostructure, the constructed Fe_xN@C/S cathode demonstrated a fairly high discharge capacity of 1085 mAh g^{-1} at 0.5 C initially, and a remaining value of 930 mAh g^{-1} after 200 cycles. In addition, it exhibits an excellent rate capability with a high initial discharge capacity of 889.8 mAh g^{-1} at 2 C. This facile PIL-to-nanocarbon synthetic approach is applicable for the exquisite design of complex hybrid carbon nanostructures with potential use in electrochemical energy storage and conversion.

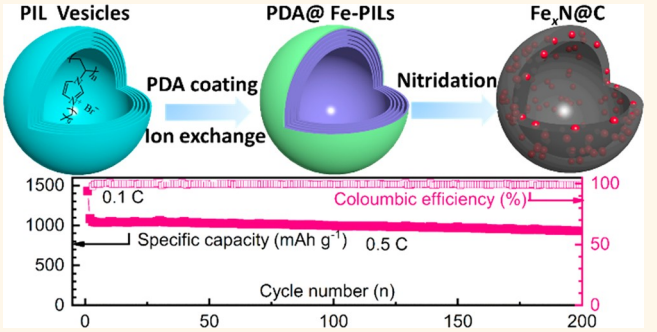

KEYWORDS: *poly(ionic liquid)s, nanovesicles, sulfur host, iron nitride, Li–S batteries*

There is a persistent pursuit of cost-effective energy storage and conversion devices of high energy density for the large-scale deployment of electric vehicles and intermittent renewable energy sources. In this context, lithium–sulfur (Li–S) batteries are recognized as a potential next-generation solution to meet these requirements due to their large theoretical capacity (1675 mAh g^{-1}) and natural abundance, environmental friendliness, and low cost of sulfur.[1,2] Despite these advantages, the practical use of Li–S batteries has been hindered by the notorious shuttle effect of lithium polysulfides (Li_2S_n, $4 \leq n \leq 8$), as the intermediates during cycling, which are highly soluble in the ether-based electrolyte.[3,4] The shuttle behavior of Li_2S_n between the cathode and anode decreases the capacity and cycling stability and raises safety concerns,[5,6] especially when metallic lithium is used as anode.[7,8] The multiphase conversion reactions from insulating sulfur to nonconductive Li_2S suffer sluggish kinetics,[9] which results in a poor rate capability and inefficient utilization of sulfur.[10,11] In parallel, there is a large volumetric expansion of ~80% during the sulfur-to-Li_2S reaction on the cathode side, weakening the adhesion of the electrode components to the current collector that gives a fast capacity fading.[12]

Received: February 25, 2022
Accepted: June 28, 2022
Published: July 5, 2022

https://doi.org/10.1021/acsnano.2c01992
ACS Nano 2022, 16, 10554–10565

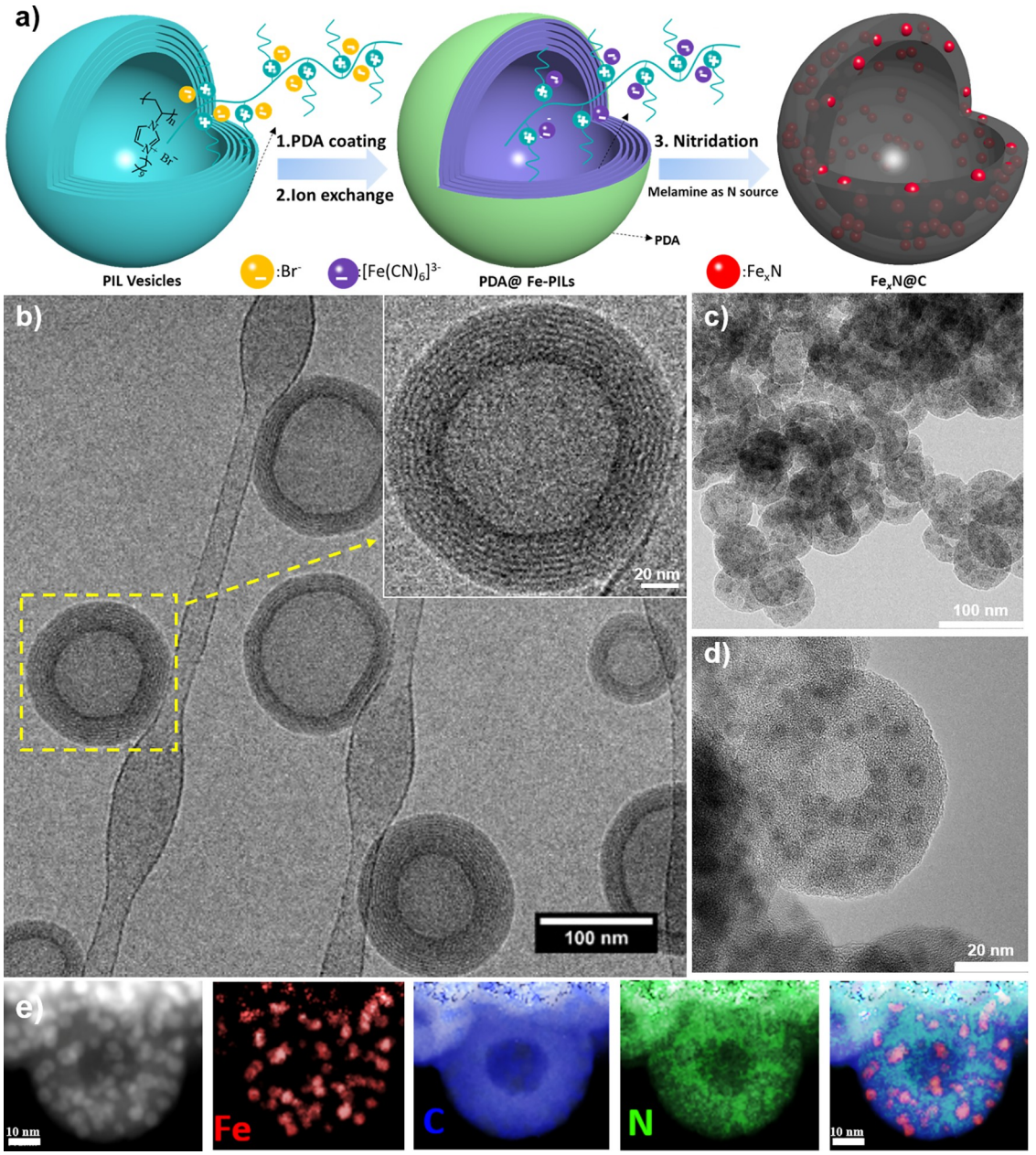

Figure 1. (a) Schematic representation of the synthesis route to Fe_xN@C nanocapsules. (b) Cryo-TEM images of the PIL nanovesicles; (c and d) TEM images of the Fe_xN@C nanocapsules. (e) STEM image and corresponding EELS mapping images of the Fe_xN@C nanocapsules.

To tackle the aforementioned issues, efforts have been devoted to improving the electrochemical performance of Li−S batteries. Significant progress has been made via impregnating sulfur into a vast variety of types of hollow as well as porous carbon-based nanomaterials with different morphologies, such as nanospheres,[13,14] nanocapsules,[15,16] nanotubes,[17,18] and nanocages.[19−21] For example, Lyu et al. prepared three-dimensional hierarchical carbon nanocages as sulfur host material with MgO as the template, which could alleviate the polysulfide dissolution issue and enhance the electron conduction and Li-ion diffusion.[19] However, it remains challenging for nanostructured carbon-based materials to effectively catalyze the multiple-step conversion reactions from LiPSs to Li_2S. Therefore, the confinement of LiPSs on-site within electrocatalytic host materials is considered the most efficient approach, since the full utilization of sulfur can be realized only when the confinement and catalytic conversion of LiPSs are integrated simultaneously.[11,22] Considering the insulating character of sulfur and polar LiPSs, nanostructured carbon/metal composites are needed and regarded as an all-in-one sulfur host to offer physical confinement, conductive matrix, and chemical adsorption.[23,24] To strengthen the interaction between the host materials and LiPSs guest, a wide range of metal compounds have been examined extensively as the LiPSs mediator, including metal oxides,[25−27] nitrides,[28,29] sulfides,[22] carbides,[30] phosphides,[31,32] and selenides.[33,34] Among them, transition-metal nitrides (TMNs) are of particular interest as electrocatalysts for the conversion of polysulfides because of their merits of superior electrical conductivity, sufficient chemical stability, and polar metal−nitrogen (M−N) bonds.[35,36] Some TMNs have been previously investigated as sulfur host materials in Li−S

https://doi.org/10.1021/acsnano.2c01992
ACS Nano 2022, 16, 10554−10565

batteries, such as TiN,[37,38] VN,[29,39,40] InN,[41] Co_4N,[42−44] MoN,[45,46] and WN.[47] For instance, Cui et al. reported a mesoporous TiN as sulfur host materials, in which the TiN-S composite cathode delivered a capacity of over 644 mAh g^{-1} after 500 cycles at 0.5 C.[38] Sun et al. developed a mesoporous VN nanorod and graphene composite, exhibiting lower polarization and faster redox reaction kinetics than that of the reduced graphene oxide cathode.[29] Meanwhile, it has been noticed that those metal-based nitride nanoparticles often suffered from high cost, low surface area, low utilization of catalytic particles, and lack of voids or space to accommodate a sufficiently large amount of sulfur.

Consequently, earth-abundant and environmentally friendly iron-based nitrides have moved into the frontline of the electrochemical field due to their high electronic conductivity and catalytic activity. Recently, yolk-shelled Fe_2N-carbon nanoboxes were designed by Sun et al. as sulfur host materials for Li−S batteries, and the polar iron nitride (Fe_2N) core could provide strong chemical bonding and effective catalytic activity for polysulfides.[48] Later on, Zhang et al. reported that phosphorus doping could boost the catalytic activity of the iron nitride (Fe_4N) nanoparticles.[49] However, the particle size of these iron nitrides was big, that is, in the range of 30−100 nm, thus suppressing the better utilization efficiency of the catalyst. Ideally, well-dispersed sub-10 nm metal-based nanoparticles could immediately expose at least 10 times more active sites for boosting the catalytic, electronic, and kinetic performance.[50,51] However, when synthesized from nanosized precursor particles, they typically tend to agglomerate and grow adversely into much larger ones during calcination.[50] Usually, time-consuming and complicated preparative routes are required, for example, the template-assisted selective etching fabrication or postloading methods.

To address this challenge, polymer−metal ion complexes as the precursor to ultrafine metal nanoparticles via one-step calcination have been actively attempted, since the parallel polymer-to-carbon conversion could in situ produce a carbonaceous matrix to impede or slow down the growth kinetics of these nanoparticles.[50,52] In this regard, imidazolium-based poly(ionic liquid)s (PILs) with N-rich ionic liquids as repeating units have been of great interest, not only because they can form N-doped porous carbon fibers or membranes with controllable N content and conductivity but also the possible coordination with the metallic species via the nitrogen atoms during pyrolysis.[53] Equally important, the introduction of metal ions into PILs can be fairly easy via the ion-complexation or ion-exchange method. Unsurprisingly, imidazolium-based PIL could produce nanostructured carbon materials embedded with metal-containing species.[54−56] Chen et al. reported carbon nanosheets with small cobalt nanoparticles by using PIL-cobaltinitrite complex/graphene oxide as precursors, which were then used to modify the separator membrane for the Li−S battery.[55] Nevertheless, due to a high density of ionic liquid species, PIL-derived carbon materials face challenges in maintaining PIL's morphology on the nanoscale. The state-of-the-art methods rely much on the time-consuming hard-template (silica) coating or silica nanocasting process.[57−59]

In this study, we developed a facile synthetic route toward structurally complex, PIL nanovesicle-templated carbon composite nanocapsules, which contain ultrafine iron nitride nanoparticles of 3−5 nm in size embedded within the carbon nanocapsules. Assisted by a protective polydopamine (PDA) coating in combination with an ion-exchange process to introduce the iron species, the hollow spherical morphology of PIL nanovesicles has, despite an inevitable dimensional shrinkage to some extent due to a large weight loss, been preserved along with pyrolysis and successfully transferred into the functional composite product. The designed nanocomposite has served as an efficient sulfur host material for Li−S batteries with drastically improved electrochemical performance. The catalytic and conductive iron nitride nanoparticles possessed abundant active sites to assist LiPS conversion and Li_2S nucleation during cycling. Besides, our synthetic route could be applied to fabricate other metal compounds (nitrides, sulfides, and phosphides) with similar nanostructures for a broader range of electrochemical applications, that is, in fuel cells and supercapacitors.

RESULTS AND DISCUSSION

The scheme in Figure 1a describes the synthetic route to the target composite, that is, iron nitride nanoparticle-functionalized carbon nanocapsules. First, PIL nanovesicles were synthesized by one-step radical homopolymerization of the monomer 3-*n*-decyl-1 vinylimidazolium bromide (ILM-10) in water at 75 °C using VA-86 as initiator under nitrogen atmosphere. After purification by dialysis, a stable PIL colloidal dispersion was obtained with a solid concentration of 10 g L^{-1}. The PIL nanoparticles exhibit a characteristic vesicular shape, as sketched in Figure 1b, with an outer diameter of 100 ± 10 nm. Interestingly, the PIL nanovesicle consists of several repeated lamellas in its wall. The alternating light and dark nanodomains stem from the hydrophobic alkyl chains and the charged backbones, respectively, due to a higher electron density of the bromide anions than that of the alkyl chains.[60] The distribution of the bromide anions (the dark lamellae) across the entire wall is a beneficial feature, as they will be anion-exchanged with ferricyanide that will be also evenly dispersed all over the wall. Besides, the SEM image of the PIL nanovesicles is further demonstrated in Figure S1. It is found that after the drying process, the morphology of some PIL nanovesicles is partially deviated from their original spherical shape, and occasionally a bowl-like structure can be observed. According to the previous report, the deformation of certain vesicles is caused expectedly by the loss of the structural water component as well as the softness of the PIL outer layer to withstand the capillary force exerted on the vesicles.[61,62] To avoid ionic cross-linking of the PIL nanovesicles possibly by ferricyanide during anion exchange, a thin protective layer of PDA was coated by in situ polymerization onto the surface of the PIL nanovesicles. The existence of the PDA layer can help preserve the nanomorpholoy of PIL during calcination because the fluidic fragmentation intermediates of PIL during carbonization may cause the amalgamation of individual PIL nanovesicles together to forfeit their nanoscopic morphology.[63] As shown in Figure S2, after deposition of a PDA layer in a Tris HCl buffer (pH = 8.5) aqueous solution, PDA@PIL dispersion turned dark, and the multilamellar pattern in the wall of the PIL nanovesicle remains (Figure S3a). Due to the dynamic feature of ionic bonds, ion exchange has been widely applied to introduce alien metal atoms into PIL.[55,56] Here, the anionic ferricyanide ions were chosen to exchange with bromide ions in the polyimidazolium-based vesicles. As depicted in Figure S4, the element mapping images of the anion-exchanged product, PDA@Fe-PIL nanovesicles, visualize the homogeneous distribution of iron atoms with a low Br

https://doi.org/10.1021/acsnano.2c01992
ACS Nano 2022, 16, 10554−10565

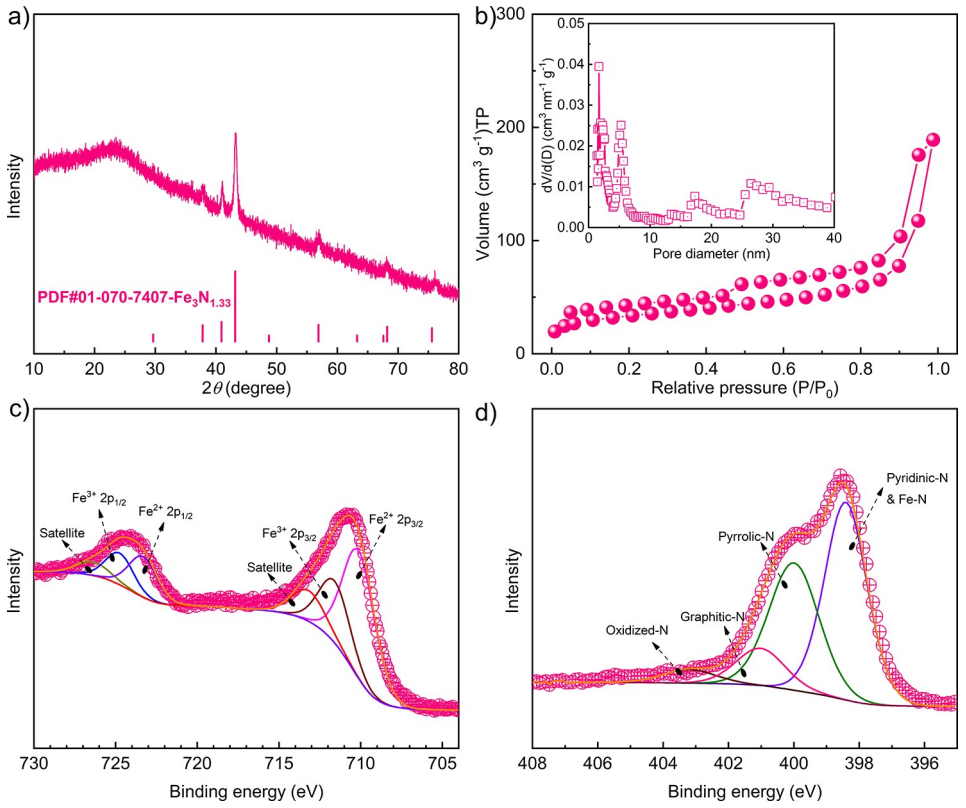

Figure 2. (a) XRD pattern, (b) nitrogen adsorption−desorption isotherms with the inset corresponding to the pore size distribution plot. XPS spectra of (c) Fe 2p and (d) N 1s of the sample Fe_xN@C.

atom content, indicating the successful introduction of iron-containing anions into the PIL nanovesicles. Besides, after anion exchange, there is no noticeable change in the PIL vesicle structure as depicted in the cryo-transmission electron microscopy (TEM) (Figure S3b) and scanning electron microscopy (SEM) image (Figure S5a).

After the nitridation, the morphology of the Fe_xN@C sample was visualized by SEM and TEM. The SEM image in Figure S5b supports that the Fe_xN@C particles inherit a similar morphology to the PIL vesicle template. The TEM images of the Fe_xN@C sample in Figure 1c,d show the as-prepared hybrid carbon product, here the visible nanocapsules of ∼50 nm in diameter and 15−25 nm in thickness and the fine iron nitride nanoparticles of 3−5 nm in size are found well-dispersed all over the hollow carbon shell. Furthermore, a scanning transmission electron microscopy (STEM) image of the Fe_xN@C sample with the corresponding electron energy-loss spectroscopy (EELS) elemental mapping of Fe, C, and N is demonstrated in Figure 1e. It is found that the N-content near the carbon nanocapsule inner layer is higher than that of the outer layer. This observation could be ascribed to the imidazole-based PILs as the carbon source, which could preserve a higher N content than that of PDA. The crystalline structure of Fe_xN@C calcinated at 500 °C is further characterized by X-ray diffraction (XRD) and HRTEM. The XRD pattern in Figure 2a can be well-indexed to the hexagonal phase of iron nitride ($Fe_3N_{1.33}$, PDF01-070-7407). The lattice fringes of the iron nitride particles are clearly observed in the HRTEM images (Figure S6). The interplanar distance is measured to be 0.31 nm, corresponding to the (101) facet of $Fe_3N_{1.33}$.[64] The effect of the calcination temperature on the formation of iron nitride particles has been studied, and the results are presented in Figure S7. It is found that the formation of the iron nitride phase is temperature-specific, that is, it can only be obtained at 500−600 °C. Beyond 700 °C, a metallic iron phase emerges. Moreover, Figure S8 reveals that the iron nitride obtained at 600 °C exhibits a larger particle size of 20−70 nm than that at 500 °C. From here on, only the iron nitride obtained at 500 °C was used in the rest work.

The effect of PDA coating, ferricyanide ions, and melamine on the morphology of the PILs nanovesicles-derived carbon calcinated at 500 °C was investigated systematically (Figure S9). Obviously, without a PDA coating, only irregularly shaped bulk carbon embedded with metal-containing nanoparticles is obtained, as shown in Figure S9a. Similarly carbon bulk (Figure S9b) is collected when calcinating the iron-free PDA@PIL nanovesicles under the same carbonization. The irregular morphology of carbon is due to the convergence of the PIL particles in a softened state at elevated temperature and could not hold their vesicular shape. Melamine as a nitrogen source was also found important to maintain the rather small size of the iron nitride nanoparticles. Without melamine, the nanocapsule shape of carbon is still nicely obtained, but in them, only a few large iron-based particles in size of 7−20 nm are embedded (Figure S9c). Similar to a previous report, the good dispersity of iron nitride nanoparticles stems from the N species in the melamine and imidazole-ring that act as anchoring site points to the metallic species.[52] Furthermore, the iron content inside the Fe_xN@C nanocapsules is 22.7 wt %, calculated from the Fe_2O_3 residual based on the thermogravimetric analysis (TGA) result in Figure S10. The metal-free carbon nanocapsules (Figure S9d) have been obtained by etching the iron nitride particles out of the Fe_xN@C sample via acid treatment. Based on the TEM

https://doi.org/10.1021/acsnano.2c01992
ACS Nano 2022, 16, 10554−10565

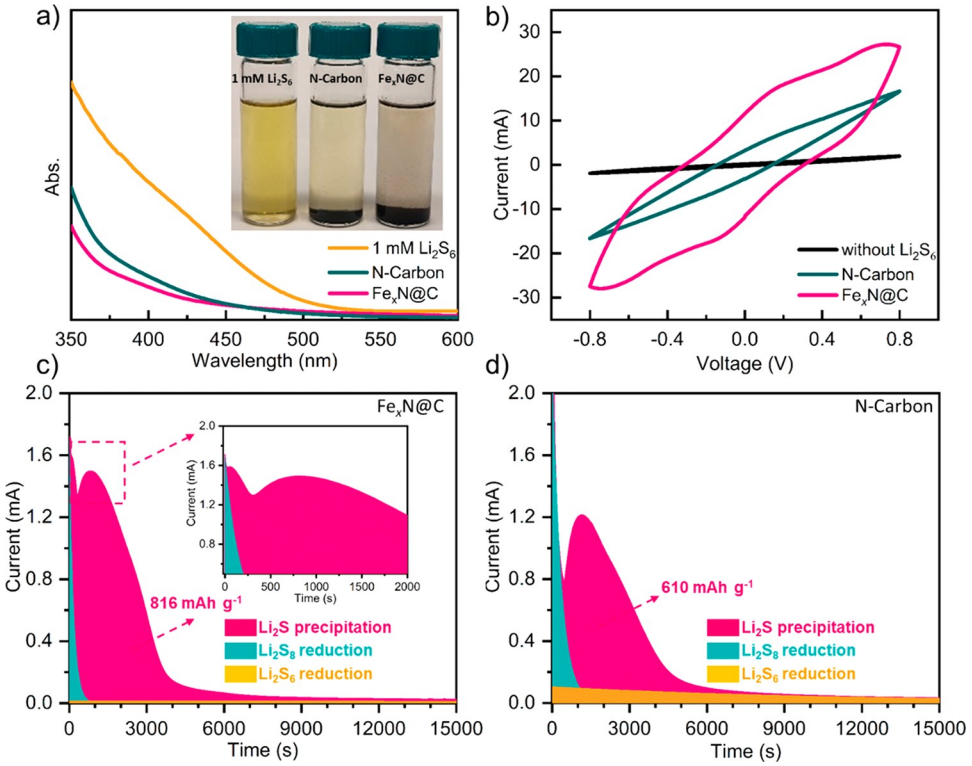

Figure 3. (a) Static adsorption for the Li_2S_6 solution by N-Carbon and Fe_xN@C with the UV−vis spectra of the corresponding supernatants, respectively. (b) CV curves at a scan rate of 10 mV s^{-1} from −0.8 to 0.8 V of the symmetric batteries with different electrodes as noted in figure, with and without the presence of Li_2S_6. The Li_2S precipitation test on different electrodes: (c) Fe_xN@C and (d) N-Carbon.

analysis and TGA result in Figures S9 and S10, iron nitride particles are removed after the repeated acid etching process.

To measure the specific surface area and pore size distribution of Fe_xN@C, the N_2 adsorption−desorption measurement at 77 K was conducted. A hysteresis loop can be observed in Figure 2b, which resembles a typical type-III isotherm. The pore size distribution diagram in the inset of Figure 2b shows that Fe_xN@C nanocapsules possess mesopores of a multimodal pore size distribution that peaks at 5, 17, and 22 nm. The 5 nm mesopores may be related to the pore inside the carbon shell, while the larger mesopores of 17 and 22 nm may stem from the hollow voids inside the carbon nanocapsules. The existence of mesopores in the Fe_xN@C sample is favorable for the sulfur loading, and their surface can also serve as the physical adsorption reservoir for LiPSs, mitigating the shuttling effect. Based on the Brunauer−Emmett−Teller (BET) equation, the specific surface area of the Fe_xN@C sample is 120 m^2 g^{-1}, while 233 m^2 g^{-1} for the N-Carbon sample due to the removal of iron nitride particles that has a higher density than carbon, as shown in Figure S11. The X-ray photoelectron spectroscopy (XPS) was applied to extract structure information on the surface composition and valence state in the Fe_xN@C nanocapsules. The high-resolution Fe 2p and N 1s spectra of the Fe_xN@C sample are displayed in Figure 2c,d, respectively. For the Fe 2p spectrum, two peaks at 723.4 and 710.3 eV are found and assigned to Fe $2p_{1/2}$ and Fe $2p_{3/2}$ of Fe^{2+} states, respectively; the Fe $2p_{1/2}$ and Fe $2p_{3/2}$ of Fe^{3+} are found located at 724.8 and 711.8 eV, respectively.[65] In addition, the peaks at 713.4 and 726.5 eV are satellite peaks. The coexistence of Fe^{3+}/Fe^{2+} is due to the surface oxidation of the iron nitride nanoparticles when they are exposed to air. Nitrogen doping into the carbon material can provide multiple favorable effects here, that is, to enhance the electrical conductivity and offer more active sites for the chemical confinement of LiPSs.[66] The N 1s spectrum in Figure 2d can be deconvoluted into four peaks at 398.1, 400.2, 401.1, and 403.2 eV, corresponding to the pyridinic, pyrrolic, graphitic, and oxidized N species, respectively.[67] It is worth noting that the peak of the pyridinic N includes the contribution of the Fe−N since the binding energy of N−Fe is close to that of the pyridinic N.[68,69]

To analyze the adsorption capability of Fe_xN@C to the LiPSs, the adsorption tests were conducted. The inset of Figure 3a shows the result of the Li_2S_6 adsorption tests of Fe_xN@C and N-Carbon particles. Six mL of Li_2S_6 solution (1 mM) in a mixture solvent DME/DOL (v/v = 1/1) was added into vials with different host materials (N-Carbon and Fe_xN@C). To study the affinity of each material to LiPSs, the same surface area of 2 m^2 based on the obtained specific surface area has been applied. After aging for 6 h in a glovebox, the color of the supernatant of the Fe_xN@C sample turned from yellow to colorless, indicative of their strong adsorption capability to extract LiPSs from solution to solid. By contrast, the color of the supernatant with metal-free carbon nanocapsules was light yellow, suggesting a weaker affinity to LiPSs. The UV−vis spectra of the two supernatant solutions in Figure 3a were recorded, and their comparison confirms that the Li_2S_6 concentration in the Fe_xN@C sample solution is reduced notably. To analyze the adsorption capability of Fe_xN@C to the LiPSs, we performed high-resolution XPS analysis of the Fe_xN@C particles before and after adsorption of Li_2S_6, and the results are shown in Figure S12. An obvious blue shift can be observed in the Fe 2p spectra after adsorption of Li_2S_6, which is highlighted with the dotted lines to show the difference

https://doi.org/10.1021/acsnano.2c01992
ACS Nano 2022, 16, 10554−10565

between the two XPS spectra. In addition, a weak shoulder peak at 708 eV in the Fe $2p_{3/2}$ region of Fe_xN@C−Li_2S_6 can be distinguished and allocated to the Fe−S binding.[70] The blue shift in the Fe 2p spectrum of Fe_xN@C−Li_2S_6 suggests that the iron nitride particles indeed provide a strong chemical interaction toward LiPSs.[71] The formation of Fe−S binding in the Fe_xN@C−Li_2S_6 indicates the electrons of sulfur atoms in the polysulfide molecules are transferred to the iron atoms, which could reduce the energy barrier for the conversion of LiPSs to Li_2S.[72,73]

The catalytic effects of Fe_xN@C on the conversion reaction of LiPSs to Li_2S were investigated in a symmetrical test cell by cyclic voltammetry (CV) method, as shown in Figure 3b. Since the Li_2S_6-free symmetrical cell only exhibits a minor contribution from the capacitive current, the polarization profiles of cells with the other two electrodes are assigned to the redox current of Li_2S_6. It can be observed that the current density significantly increases when Fe_xN@C and N-Carbon nanocapsules were used as the electrodes, demonstrating that both iron nitride and hollow carbon nanocapsules can significantly facilitate the electrochemical reactions of LiPSs. The larger area of the CV curves in the Fe_xN@C electrode than that of the carbon nanocapsules suggests considerable improvement in the redox kinetics of LiPSs conversion reactions in a liquid phase ($Li_2S_8 \leftrightarrow Li_2S_6 \leftrightarrow Li_2S_4$) by introducing iron nitride nanoparticles into carbon nanocapsules.[9] To further explore the catalytic properties of the Fe_xN@C nanoparticles, Li_2S nucleation was investigated with the potentiostat discharging method.[74] As observed in Figure 3, the presence of Fe_xN@C notably results in faster nucleation and growth and a higher discharging peak current during potentiostatic discharge at 2.05 V vs Li/Li^+. Based on Faraday's law, the discharge capacity of the Fe_xN@C electrode was 816 mAh g^{-1}, which is higher than that of the N-Carbon electrode (610.1 mAh g^{-1}). Apart from this observation, the current peak position during the Li_2S precipitation process at Fe_xN@C is located at 52 s, which is much earlier than that for the N-Carbon electrode. This result suggests that iron nitride nanoparticles can boost the kinetics of the Li_2S precipitation process during cycling.

Furthermore, first-principle simulations based on density functional theory (DFT) were applied to theoretically study the binding energy, structures, and motifs of LiPSs (Li_2S_2, Li_2S_4, Li_2S_6, and Li_2S_8) molecules on the surfaces of three common iron nitrides (Fe_2N, Fe_3N, and $Fe_3N_{1.33}$). The binding energy of LiPSs (Li_2S_n with n = 2, 4, 6, and 8) on varied iron nitride surfaces (Fe_2N, Fe_3N, and $Fe_3N_{1.33}$) was calculated via the formula $E = E_{Li_2S_n-Fe_xN\ complexes} - E_{Li_2S_n} - E_{Fe_xN}$, in which $E_{Li_2S_n}$, E_{Fe_xN}, and $E_{Li_2S_n-Fe_xN}$ complexes are the total energies of Li_2S_n molecules, iron nitride surfaces, and the adsorption of Li_2S_n on iron nitride surfaces with optimized adsorption structure, respectively. A more negative value indicates a much stronger adsorption capability of LiPSs species on the given iron nitride surfaces. As demonstrated in Figure 4a and Figure S13, the calculated binding energies for Li_2S_x species with a given iron nitride can be described by Li_2S_6 > Li_2S_8 > Li_2S_4 > L_2S_2, and the iron nitride $Fe_3N_{1.33}$ exhibits a better adsorption capability to long-chain LiPSs than the other two ones. For instance, the calculated surface adsorption energies for a Li_2S_6 molecule on the iron nitrides are 4.39, 4.89, and 5.01 eV for Fe_2N, Fe_3N, and $Fe_3N_{1.33}$, respectively. It is worth noting that the obtained binding energies of different

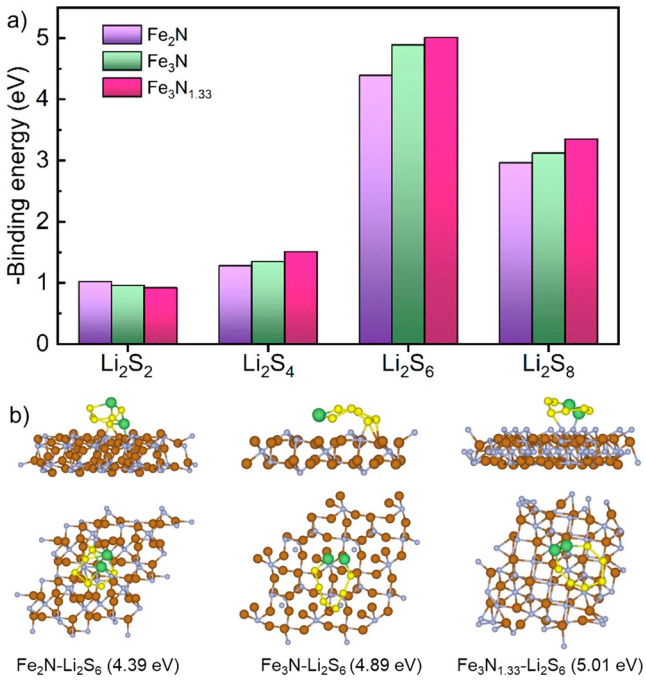

Figure 4. DFT calculations: (a) the binding energy of different LiPSs molecules (Li_2S_2, Li_2S_4, Li_2S_6, and Li_2S_8) on the surfaces of different iron nitrides (Fe_2N, Fe_3N, and $Fe_3N_{1.33}$). (b) The optimized binding configurations of the Li_2S_6 molecule on the surfaces of different iron nitrides, as noted in the figure.

LiPSs on Fe_2N are well consistent with those determined from previous DFT calculations,[48] indicating the good reliability of the applied calculated methods. The higher binding energy indicates a better chemical trapping capability of soluble Li_2S_6 and Li_2S_8 species on the $Fe_3N_{1.33}$ electrode, which could substantially mitigate the shuttle effect of LiPSs. A further inspection of the optimized binding structures of the Li_2S_6 molecule on the $Fe_3N_{1.33}$ demonstrates that the Li_2S_6 molecule is more likely to coordinate with the nitrogen atoms on the iron nitride through the interaction between lithium and nitrogen. In contrast, the sulfur atoms of Li_2S_6 have strong interactions with the central Fe atoms surrounded by N atoms. Besides, Li_2S_6 molecules on the iron nitride surfaces tend to be curved or bent rather than stretched, which could be favorable for breaking long polysulfides into shorter ones during cycling.

To demonstrate the structural merits of the hollow Fe_xN@C, a sulfur-loaded composite of Fe_xN@C/S was prepared by the melting diffusion method and used as cathode materials for Li−S batteries. The specific sulfur contents inside the composites are 72.1 wt % for Fe_xN@C/S and 72.6 wt % for N-Carbon/S, respectively, which are determined by TGA (Figure S14). The CV measurements were conducted in a cell voltage range of 1.7−2.8 V vs Li/Li^+ at a scanning rate of 0.1 mV s^{-1}. Two representative sharp peaks are observed in the first cathodic scan as shown in Figure 5a. The first peak around 2.25 V corresponds to the reduction of sulfur to long-chain LiPSs (Li_2S_n), and the other is ascribed to the reduction of LiPSs to short-chain lithium sulfides (Li_2S_2/Li_2S). During the successive anodic scanning, the two oxidation peaks (2.39 and 2.44 V) can be assigned to the reversible conversion of Li_2S to LiPSs and finally to sulfur. To note, the peak position of Fe_xN@C in the cathodic scan is shifted to a higher electrode potential, while in the anodic scan, it moves to a lower electrode potential, indicating the lower polarization of the

https://doi.org/10.1021/acsnano.2c01992
ACS Nano 2022, 16, 10554−10565

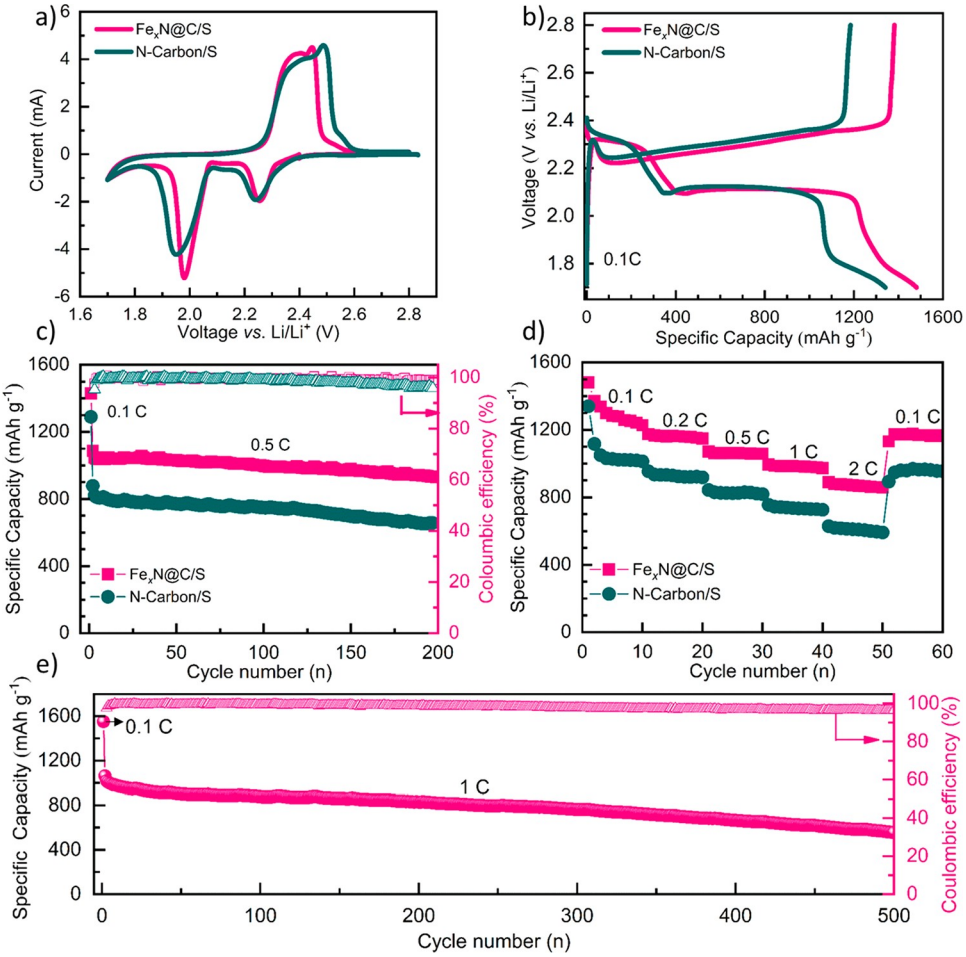

Figure 5. (a) CV curves scanned at 0.1 mV s^{-1}, (b) discharge−charge curves at 0.1 C (1 C = 1675 mA g^{-1}), (c) cycling stability at 0.5 C, and (d) rate capability of the Li−S batteries with Fe$_x$N@C/S and N-Carbon/S as the cathode. (e) Long-term cycling performance at 1 C of the Li−S batteries with Fe$_x$N@C/S as the cathode. All measurements have been performed in the range of 1.7−2.8 V vs Li/Li$^+$.

battery with Fe$_x$N@C as the host materials compared with the carbon nanocapsules. This could be ascribed to the high conductivity and the catalytic effect of the ultrafine iron nitride particles inside the carbon nanocapsules. The initial charging−discharging curves of these two electrodes at 0.1C are given in Figure 5b. The initial specific discharge capacity of the Fe$_x$N@C/S electrode is 1481.5 mAh g^{-1}, which is much higher than that of the N-Carbon/S (1345 mAh g^{-1}). Two characteristic plateaus in the discharge curve are observed at around 2.3 and 2.1 V for both studied electrodes, corresponding to the conversion reactions from sulfur to LiPSs and their further reduction to lithium sulfide, respectively. The cycling performance of Li−S batteries with different sulfur host materials was further measured at 0.5 C (Figure 5c). The initial discharge capacity of the N-Carbon/S electrode was 878.9 mAh g^{-1} at 0.5 C. After 100 cycles, it still capable of delivering a capacity of 748.8 mAh g^{-1}, which is much higher than that of the previous carbon nanocapsule/sulfur composites.[15] This could be ascribed to nitrogen-rich carbon derived from PDA and PILs, which can offer rich sites to chemically anchor LiPSs. Combined with the synergistic chemical adsorption and catalytic effect of iron nitride particles and the physical confinement of the carbon nanocapsules to suppress the shuttle effect, the Fe$_x$N@C/S electrode shows excellent cycling stability and delivers a high initial discharge capacity of 1085 mAh g^{-1} at 0.5 C with a remaining value of 930 mAh g^{-1} after 200 cycles, which is much higher than its counterparts. To confirm the structural robustness of the nanocapsule particles, the Fe$_x$N@C/S electrode after cycling was washed with CS_2 and ethanol and imaged with TEM. As shown in Figure S15, the Fe$_x$N@C particles still maintained nanocapsular morphology without breaking down, suggesting good structural robustness.

The rate capabilities of Fe$_x$N@C/S and N-Carbon/S electrodes were measured at different current densities and displayed in Figure 5d. After 10 cycles at each current, the retained discharge capacities of Fe$_x$N@C/S electrode are 1226.9, 1148.7, 1057.6, 973.8, and 858.1 mAh g^{-1}at 0.1, 0.2, 0.5, 1, and 2 C, respectively. Under the same conditions, the N-Carbon/S electrode delivers a remaining capacity of 1012.5, 918.0, 818.9, 725.4, and 591.4 mAh g^{-1} at 0.1, 0.2, 0.5, 1, and 2 C, respectively. Since the iron nitride particles inside carbon nanocapsules can facilitate the conversion reaction from LiPSs to Li_2S, it is expected that the Fe$_x$N@C/S electrode exhibits a better rate capability than that of the N-Carbon/S electrode. Meanwhile, the EIS results in Figure S16 prove that the coin cell with Fe$_x$N@C/S electrode exhibits a lower charge-transfer resistance than that with N-Carbon/S, which could be contributed to its better rate capability. From the charge/discharge voltage profiles of the Fe$_x$N@C/S electrode at different current densities in Figure S17, the charge platforms shifted positively, and the discharge platforms shifted

https://doi.org/10.1021/acsnano.2c01992
ACS Nano 2022, 16, 10554−10565

negatively with the increasing rate, which is attributed to the polarization. Moreover, the two typical discharge plateaus are present even when the current density increases to 2 C, suggesting the fast redox kinetics of the Fe_xN@C electrode due to the high conductivity and catalytic effect of iron nitride particles. Finally, the long-term cycling stability of the Li−S battery with the Fe_xN@C/S electrode has been tested and demonstrated in Figure 5e. After the activation at 0.1 C for one cycle, the Fe_xN@C/S electrode shows an initial discharge capacity of 1061 mAh g^{-1} at 1 C, which is higher than that of the recently reported metal nitrides summarized in Table S1. Although direct comparison in electrochemical performances among different systems is not reasonable due to the different fabrication parameters, the comparable results in this work suggest our unique composite nanostructure with pregnated fine iron nitride particles could improve the sulfur utilization efficiency even at a high C-rate. After 500 cycles, it continues to deliver a discharge capacity of 556.5 mAh g^{-1} with an average fading rate of 0.095% per cycle, indicating the potential of Fe_xN@C nanocapsules to promote the applications of Li−S batteries.

CONCLUSIONS

In summary, structurally exquisite carbon nanocapsules were successfully templated from morphologically similar poly(ionic liquid) nanovesicles assisted by the PDA coating and ion exchange, a method to prepare their carbon/iron nitride composite nanocapsules. Because of the unique hollow nanostructure, the obtained carbon nanocapsules embedded with ultrafine iron nitride nanoparticles worked as an efficient sulfur host material for the Li−S battery. The large voids in the nanocapsules accommodate a large amount of sulfur loading (70 wt %) and mitigate the volumetric expansion during the cycling process. The iron nitride nanoparticles were found to significantly facilitate the LiPSs to Li_2S conversion during the discharging process due to their high conductivity and catalytic activity. Based on the DFT calculation and adsorption test, Fe_xN@C nanocapsules exhibited a strong ability to confine LiPSs due to a high chemical binding energy of iron nitride nanoparticles and the physical confinement of carbon nanocapsules. Benefiting from those advantages, the Fe_xN@C/S electrode delivered a high initial discharge capacity of 1085 mAh g^{-1} at 0.5 C with a remaining value of 930 mAh g^{-1} after 200 cycles; it also exhibited a high rate capability with the initial discharge capacity of 889.8 mAh g^{-1} at 2 C. We believe that the synthetic route developed in this work can serve to obtain structurally well-defined porous carbon nanomaterials functionalized with metal-based compounds, and they are expected to meet electrochemical applications beyond batteries.

METHODS

Materials. Sublimed sulfur powder, lithium nitrate ($LiNO_3$), dopamine hydrochloride, potassium ferricyanide (III), anhydrous ethanol, bis(trifluoromethane)sulfonimide lithium salt (LiTFSI), polyvinylidene fluoride (PVDF), *N*-methyl-2-pyrrolidone (NMP), 1-vinylimidazole (≥99%), 1-bromodecane (98%), 1,2-dimethoxyethane (DME), carbon disulfide, tris(hydroxymethyl) aminomethane (Tris), and 1,3-dioxolane (DOL) were purchased from Sigma-Aldrich. Hydrochloric acid solution (37%) and melamine were purchased from Alfa-Aesar. Water-soluble nonionic azo initiator 2,2′-azobis[2-methyl-*N*-(2-hydroxyethyl) propionamide] (VA086) was obtained from Wako Chemicals. All chemicals were used without any further purification.

Synthesis of Ionic Liquid Monomer and Hollow PIL Nanocapsules. According to the previous report,[S8] the monomer 3-*n*-decyl-1-vinylimidazolium bromide (ILM-10) was synthesized by dissolving 0.1 mol of 1-vinylimidazole and 0.1 mol of decyl bromide into 30 mL of methanol. Then, the mixture was stirred at 60 °C for 15 h. After cooling down, the reaction mixture was added dropwise into 1 L of diethyl ether. The white precipitate was filtered off and dried under vacuum at room temperature. The polymerization of ILM-10 monomer to form hollow PIL nanovesicles was based on our previous report with minor changes.[75] Specifically, 1 g of the monomer ILM-10 and 150 mg of water-soluble initiator VA086 were dissolved in 100 mL of water inside a 250 mL Schlenk flask. The air inside the Schlenk flask was replaced by argon by three freeze−pump−thaw cycles. Afterward, it was put into an oil bath and stirred at 75 °C for 24 h. After being cooled down to room temperature, a stable translucent dispersion was obtained. The stable dispersion was then purified via dialysis against deionized water (>10-fold volume) for 3 days, replacing the water every 12 h.

Synthesis of Polydopamine-Coated PIL Nanovesicles (PDA@PIL). First, 41.2 mL of the colloidal PIL solution (solid content: 9.7 mg mL^{-1}) was diluted into 158.8 mL by water under sonication in 15 min. Then, 0.21g of Tris powder was added into the solution above, and the pH value was adjusted to ∼8.5 with the desired amount of the concentrated HCl solution (37%). After that, 100 mg of dopamine hydrochloride was added to the solution. During the initial dopamine polymerization process, the solution was treated by sonication for 2 h at room temperature. Afterward, it was magnetically stirred at room temperature for 15 h. Finally, the colloidal dispersion of the PDA-coated PIL nanovesicles was purified via dialysis.

Template Synthesis of Carbon Nanocapsules Functionalized with Iron Nitride Nanoparticles. After dialysis, the volume of the above-mentioned PDA@PIL nanovesicle dispersion was adjusted to 300 mL in a round-bottom flask. After a sonication treatment for 15 min, 0.494 g of potassium ferricyanide ($K_3[Fe(CN)_6]$) was added into the dispersion. Along with sonication treatment for 1 h, the flask was sealed and put into an oil bath at 60 °C for the ion exchange for 24 h. After naturally cooling down to room temperature, it was vacuum filtered off and washed with water three times. The obtained sample was freeze-dried and termed PDA@Fe-PIL. 200 mg of PDA@Fe-PIL powder was placed in an alumina crucible at the center of the tube furnace, and 3 g of melamine powder was placed in another alumina crucible, which was positioned upstream of PDA@Fe-PIL powder. The sample PDA@Fe-PIL was calcinated at 500 °C at a heating rate of 5 °C min^{-1} for 2 h and then naturally cooled down to room temperature under an Ar flow. The obtained sample was termed Fe_xN@C.

Synthesis of Nanovesicle-Templated Hollow Carbon Nanocapsules and Bulk Carbon Particles. The hollow carbon nanocapsule sample was synthesized by etching off the iron nitride nanoparticles by a HCl solution (4 M) at 60 °C for 15 h. After washing with water and ethanol three times, the etching process was repeated twice to ensure no iron nitride particles were left. Then, the collected hollow carbon nanocapsules were dried at 60 °C under vacuum, termed as "N-Carbon". The bulk carbon particles (Bulk-Carbon) were obtained by the calcination of PDA@PIL powder under the same condition as that of Fe_xN@C nanocapsules.

Adsorption Test of Lithium Polysulfides. A Li_2S_6 solution was prepared by dissolving stoichiometric sulfur and Li_2S (5:1, in molar ratio) in a mixed solvent of DOL/DME (1:1, v/v), followed by vigorous stirring at 80 °C for 48 h. Based on the N_2 adsorption−desorption isotherm analysis, Fe_xN@C and carbon nanoparticle powders with the same specific surface area were added into 6 mL of Li_2S_6 solution (1 mM), respectively. After aging for 6 h in a glovebox, the supernatant liquid was centrifuged and sealed in the quartz cuvette for the UV−vis spectroscopy test.

Kinetics of Li_2S Precipitation. Initially, the slurry of the host materials (Fe_xN@C or N-Carbon), Ketjen black, and PVDF (8:1:1 weight ratio) in NMP was cast on the carbon paper. After drying at 60 °C under vacuum, the electrode was cut into wafers with a diameter of

https://doi.org/10.1021/acsnano.2c01992
ACS Nano 2022, 16, 10554−10565

14 mm. The areal loading of host materials is around 1 mg cm^{-2}. The cell was assembled using 20 μL of Li_2S_8 (0.25 M) solution with 1.0 M LiTFSI in the mixture solvent of DOL and DME (1:1, v/v) as catholyte, and 20 μL electrolyte without Li_2S_8 was used as anolyte. For the Li_2S precipitation process, the assembled cells were first discharged galvanostatically at a C-rate of 0.1 C to 2.16 V *vs.* Li/Li^+ and then discharged potentiostatically at 2.05 V vs Li/Li^+ for Li_2S nucleation and growth. The potentiostat discharge was terminated after 65000 s.

Kinetic Evaluation of Polysulfide Conversion. Two identical electrodes, the same as the one for the Li_2S precipitation test, were used as the working and the counter electrode, respectively. 40 μL of Li_2S_6 (2.5 M, based on sulfur content) solution with 1.0 M LiTFSI in the solvent of DOL and DME (1:1, v/v) was used as electrolyte. The assembled symmetric battery was measured at a scan rate of 10 mV s^{-1} in a potential window from −0.8 to 0.8 V.

Preparation of the Cathodes. The Fe_xN@C and sulfur powder in a weight ratio of 7:3 were first mixed with the assistance of carbon disulfide. After the solvent was completely evaporated, the mixture was sealed in an autoclave under argon and heated at 155 °C for 12 h. Then, the electrode was prepared by casting the slurry of Fe_xN@C/sulfur, Ketjen black, and PVDF (7:2:1 in weight ratio) on a carbon paper by the doctor blade technique. After drying at 50 °C under vacuum overnight, the electrode was cut into wafers with a diameter of 14 mm. The areal sulfur loading of the electrode is around ∼1.5 mg cm^{-2}.

Electrochemical Measurement. CR2025-type coin cells were assembled with the cathodes, Li foil as the anode, and a piece of Celgard 2700 membrane as the separator in an Ar-filled glovebox (UNIlab plus, M. BRAUN) with H_2O content <0.5 ppm and O_2 content <0.5 ppm. One M LiTFSI in DME/DOL (1:1 v/v) with 2 wt % of $LiNO_3$ was used as the electrolyte solution. The volume of electrolyte for each cell was 40 μL. Before electrochemical tests, all assembled cells were aged under open circuit potential for 12 h at room temperature to allow the electrolyte to wet the electrode. In this work, the current density of 1 C equals 1675 mA g^{-1}. The specific capacity is calculated based on the mass of sulfur content in the electrode. Galvanostatic discharging−charging was conducted on a Neware battery testing system (CT-4008-5 V10 mA) at room temperature. The electrochemical impedance spectroscopy (EIS) was recorded on GAMRY Interface 1000 within a frequency range of 100 kHz to 0.01 Hz. The cyclic voltammetry (CV) curves were measured with a Biologic VMP3 electrochemical workstation with a scanning rate of 0.1 mV s^{-1} in the electrochemical window of 1.7−2.8 V vs Li/Li^+.

Density Functional Theory Calculations. Density functional theory (DFT) calculations were performed using the projector augmented wave method that has been implemented in Vienna ab initio Simulation Package. The Perdew−Burke−Ernzerhof exchange−correlation function was adopted, the cutoff energy for this plane-wave basis set was set to be 450 eV, and 5 × 5 × 1 Γ-centered *k*-point grids were used for Brillouin zone integrations.

The (111) crystalline surface of Fe_2N, Fe_3N, and $Fe_3N_{1.33}$ electrodes was modeled by the periodic slab repeated in 2 × 2 surface unit cells. The bottom atom layers in these electrodes were fixed during DFT calculations to simulate bulk structures, while the top atom layers were free to simulate the surface state. A vacuum of 20 Å was contained in each modeling system to reduce interactions between each surface. The isolated Li_2S_8, Li_2S_6, Li_2S_4, and Li_2S_2 molecules were modeled in the center of a big enough cubic lattice. All structures were fully relaxed to their optimized geometries with the force convergence set to 0.01 eV/Å. To explore the lowest-energy configurations of adsorbed systems, we carefully manipulated structure parameters of the initial state (the distance, angle, and displacement between molecule and surface) to relax fully and selected the lowest-energy result as the final state for data analysis.

Material Characterizations. The morphology of the obtained samples was investigated by an LEO 1530 field emission scanning electron microscope (SEM) and a JEOL-2100 transmission electron microscopy (TEM) (JEOL, GmbH, Eching, Germany) operated at 200 kV. X-ray diffraction (XRD) patterns were collected using a Bruker D8 diffractometer with Cu K_α radiation. N_2 adsorption−desorption isotherms were conducted by using Quantachrome Autosorb-1 systems at 77 K. Specific surface areas were calculated using the Brunauer−Emmett−Teller (BET) method based on a multipoint analysis. The chemical states of the elements in the samples were characterized using X-ray photoelectron spectroscopy (XPS) with an ESCA-Lab-220i-XL X-ray photoelectron spectrometer (Thermo Fisher Scientific) with Al K_α sources ($h\nu$ = 1486.6 eV). Thermogravimetric analysis (TGA) was carried out on PerkinElmer (TGA 8000) in the temperature range of 30−900 °C at a heating rate of 10 °C min^{-1} under N_2 or in synthetic air. UV−vis spectra (300−800 nm) are measured by using Lambda 650 spectrometer supplied by PerkinElmer at 20 °C. Scanning transmission electron microscopy (STEM) characterization employing electron energy-loss spectroscopy (EELS) was performed using a Nion HERMES microscope (Nion Co., Kirkland, WA, USA). Samples for STEM-EELS analysis were prepared by depositing a drop of sample solution on lacey carbon-coated copper TEM grids (200 mesh, Electron Microscopy Sciences, Hatfield, PA) and letting them dry at room temperature. Cryo-TEM was performed with a JEOL JEM-2100 transmission electron microscope (JEOL GmbH, Eching, Germany). Cryo-TEM specimens were vitrified by plunging the samples into liquid ethane using an automated plunge freezer (Vitrobot Mark IV, FEI) set at 4 °C and 95% humidity. Approximately 5 μL of 0.025 wt % solution was deposited on a lacey carbon-coated copper grid (200 meshes, Electron Microscopy Sciences, Hatfield, PA) and equilibrated at the adjusted temperature and humidity for 2 min. After blotting the liquid, the specimens were vitrified, inserted into a precooled cryo-transfer holder (Gatan 914, Gatan, Munich, Germany), and finally transferred into the TEM which was operated at 200 kV. A defocus of the objective lens of about 0.5 μm was used to increase the contrast. Cryo-TEM micrographs were recorded with a bottom-mounted 4 × 4k CMOS camera (TemCam-F416, TVIPS, Gauting, Germany). The total electron dose in each micrograph was kept below 20 $e^-/Å^2$.

ASSOCIATED CONTENT

Supporting Information

The Supporting Information is available free of charge at https://pubs.acs.org/doi/10.1021/acsnano.2c01992.

SEM images of the PILs, PDA@Fe-PILs and Fe_xN@C. Photograph of dispersion of PIL vesicles and PDA@PIL vesicles in water. Cryo-TEM images and EDX analysis of the PDA@PIL and PDA@Fe-PIL samples. HR-TEM images of the Fe_xN@C particles. XRD of the PDA@Fe-PIL calcinated at different temperatures. TGA curves of the Fe_xN@C, N-Carbon, Fe_xN@C/S, and N-Carbon/S. TEM images of the PILs-based particles after calcination. Nitrogen adsorption−desorption isotherms of N-Carbon. DFT calculation results of LiPS molecules on different iron nitrides. Charge−discharge curves and EIS spectra of Li−S batteries. TEM image of Fe_xN@C after cycling. Performance comparison of Fe_xN@C/S electrode with other metal nitrides (PDF)

AUTHOR INFORMATION

Corresponding Authors

Yan Lu − *Department for Electrochemical Energy Storage, Helmholtz-Zentrum Berlin für Materialien und Energie, 14109 Berlin, Germany; Institute of Chemistry, University of Potsdam, 14476 Potsdam, Germany;* orcid.org/0000-0003-3055-0073; Email: yan.lu@helmholtz-berlin.de

Jiayin Yuan − *Department of Materials and Environmental Chemistry, Stockholm University, Stockholm 10691, Sweden;* orcid.org/0000-0003-1016-5135; Email: jiayin.yuan@mmk.su.se

https://doi.org/10.1021/acsnano.2c01992
ACS Nano 2022, 16, 10554−10565

Authors

Dongjiu Xie − *Department for Electrochemical Energy Storage, Helmholtz-Zentrum Berlin für Materialien und Energie, 14109 Berlin, Germany; Institute of Chemistry, University of Potsdam, 14476 Potsdam, Germany*

Yaolin Xu − *Department for Electrochemical Energy Storage, Helmholtz-Zentrum Berlin für Materialien und Energie, 14109 Berlin, Germany;* orcid.org/0000-0002-2658-3852

Yonglei Wang − *Department for Electrochemical Energy Storage, Helmholtz-Zentrum Berlin für Materialien und Energie, 14109 Berlin, Germany;* orcid.org/0000-0003-3393-7257

Xuefeng Pan − *Department for Electrochemical Energy Storage, Helmholtz-Zentrum Berlin für Materialien und Energie, 14109 Berlin, Germany; Institute of Chemistry, University of Potsdam, 14476 Potsdam, Germany*

Eneli Härk − *Department for Electrochemical Energy Storage, Helmholtz-Zentrum Berlin für Materialien und Energie, 14109 Berlin, Germany*

Zdravko Kochovski − *Department for Electrochemical Energy Storage, Helmholtz-Zentrum Berlin für Materialien und Energie, 14109 Berlin, Germany;* orcid.org/0000-0001-8375-0365

Alberto Eljarrat − *Institut für Physik and IRIS Adlershof, Humboldt-Universität zu Berlin, 12489 Berlin, Germany*

Johannes Müller − *Institut für Physik and IRIS Adlershof, Humboldt-Universität zu Berlin, 12489 Berlin, Germany*

Christoph T. Koch − *Institut für Physik and IRIS Adlershof, Humboldt-Universität zu Berlin, 12489 Berlin, Germany;* orcid.org/0000-0002-3984-1523

Complete contact information is available at: https://pubs.acs.org/10.1021/acsnano.2c01992

Notes

The authors declare no competing financial interest.

ACKNOWLEDGMENTS

The authors acknowledge Mr. J. Yang and Dr. Johannes Schmidt at Department of Chemistry/Functional Materials, Technische Universität Berlin for the XPS measurement. The computations in this work were enabled by resources provided by Swedish National Infrastructure for Computing (SNIC) at PDC, HPC2N, and NSC partially funded by Swedish Research Council through grant agreement no. 2016-07213. Dr. Y. Xu acknowledges the Humboldt Research Fellowship for Postdoctoral Researchers from the Alexander von Humboldt Foundation for financial support. Prof. J. Yuan is grateful for financial support from Swedish Research Council Grant 2018-05351, and the Wallenberg Academy Fellow program (grant KAW 2017.0166) from the Knut & Alice Wallenberg Foundation in Sweden. The authors thank Benedikt Haas for continuous maintenance, upgrades and alignments of the Nion HERMES microscope, as well as user support. Dr. A. Eljarrat, J. Müller, and C. T. Koch acknowledge funding by the Deutsche Forschungsgemeinschaft (DFG) - project no. 182087777-SFB95.

REFERENCES

(1) Ji, X.; Lee, K. T.; Nazar, L. F. A highly ordered nanostructured carbon-sulphur cathode for lithium−sulphur batteries. *Nat. Mater.* **2009**, *8* (6), 500−506.

(2) Pang, Q.; Liang, X.; Kwok, C. Y.; Nazar, L. F. Advances in lithium-sulfur batteries based on multifunctional cathodes and electrolytes. *Nature Energy* **2016**, *1* (9), 16132.

(3) Zhang, S. S. Liquid electrolyte lithium/sulfur battery: Fundamental chemistry, problems, and solutions. *J. Power Sources* **2013**, *231*, 153−162.

(4) Wild, M.; O'Neill, L.; Zhang, T.; Purkayastha, R.; Minton, G.; Marinescu, M.; Offer, G. J. Lithium-sulfur batteries, a mechanistic review. *Energy Environ. Sci.* **2015**, *8* (12), 3477−3494.

(5) Cheon, S.-E.; Ko, K.-S.; Cho, J.-H.; Kim, S.-W.; Chin, E.-Y.; Kim, H.-T. Rechargeable lithium sulfur battery: II. Rate capability and cycle characteristics. *J. Electrochem. Soc.* **2003**, *150* (6), A800.

(6) Manthiram, A.; Fu, Y.; Chung, S.-H.; Zu, C.; Su, Y.-S. Rechargeable Lithium−Sulfur Batteries. *Chem. Rev.* **2014**, *114* (23), 11751−11787.

(7) Xiong, S.; Xie, K.; Diao, Y.; Hong, X. Characterization of the solid electrolyte interphase on lithium anode for preventing the shuttle mechanism in lithium−sulfur batteries. *J. Power Sources* **2014**, *246*, 840−845.

(8) Zhang, L.; Ling, M.; Feng, J.; Mai, L.; Liu, G.; Guo, J. The synergetic interaction between $LiNO_3$ and lithium polysulfides for suppressing shuttle effect of lithium-sulfur batteries. *Energy Storage Materials* **2018**, *11*, 24−29.

(9) Yuan, Z.; Peng, H. J.; Hou, T. Z.; Huang, J. Q.; Chen, C. M.; Wang, D. W.; Cheng, X. B.; Wei, F.; Zhang, Q. Powering Lithium-Sulfur Battery Performance by Propelling Polysulfide Redox at Sulfiphilic Hosts. *Nano Lett.* **2016**, *16* (1), 519−27.

(10) Liu, D.; Zhang, C.; Zhou, G.; Lv, W.; Ling, G.; Zhi, L.; Yang, Q.-H. Catalytic Effects in Lithium-Sulfur Batteries: Promoted Sulfur Transformation and Reduced Shuttle Effect. *Advanced Science* **2018**, *5* (1), 1700270.

(11) Wang, P.; Xi, B.; Huang, M.; Chen, W.; Feng, J.; Xiong, S. Emerging Catalysts to Promote Kinetics of Lithium-Sulfur Batteries. *Adv. Energy Mater.* **2021**, *11* (7), 2002893.

(12) Wei Seh, Z.; Li, W.; Cha, J. J.; Zheng, G.; Yang, Y.; McDowell, M. T.; Hsu, P.-C.; Cui, Y. Sulphur-TiO_2 yolk-shell nanoarchitecture with internal void space for long-cycle lithium-sulphur batteries. *Nat. Commun.* **2013**, *4* (1), 1331.

(13) He, G.; Evers, S.; Liang, X.; Cuisinier, M.; Garsuch, A.; Nazar, L. F. Tailoring Porosity in Carbon Nanospheres for Lithium-Sulfur Battery Cathodes. *ACS Nano* **2013**, *7* (12), 10920−10930.

(14) Zhou, W.; Wang, C.; Zhang, Q.; Abruña, H. D.; He, Y.; Wang, J.; Mao, S. X.; Xiao, X. Tailoring Pore Size of Nitrogen-Doped Hollow Carbon Nanospheres for Confining Sulfur in Lithium-Sulfur Batteries. *Adv. Energy Mater.* **2015**, *5* (16), 1401752.

(15) Park, S.-K.; Lee, J.; Hwang, T.; Piao, Y. Sulfur-loaded monodisperse carbon nanocapsules anchored on graphene nanosheets as cathodes for high performance lithium-sulfur batteries. *Journal of Materials Chemistry A* **2017**, *5* (3), 975−981.

(16) Tan, G.; Xu, R.; Xing, Z.; Yuan, Y.; Lu, J.; Wen, J.; Liu, C.; Ma, L.; Zhan, C.; Liu, Q.; Wu, T.; Jian, Z.; Shahbazian-Yassar, R.; Ren, Y.; Miller, D. J.; Curtiss, L. A.; Ji, X.; Amine, K. Burning lithium in CS_2 for high-performing compact Li_2S-graphene nanocapsules for Li-S batteries. *Nature Energy* **2017**, *2* (7), 17090.

(17) Jin, K.; Zhou, X.; Zhang, L.; Xin, X.; Wang, G.; Liu, Z. Sulfur/Carbon Nanotube Composite Film as a Flexible Cathode for Lithium-Sulfur Batteries. *J. Phys. Chem. C* **2013**, *117* (41), 21112−21119.

(18) Dörfler, S.; Hagen, M.; Althues, H.; Tübke, J.; Kaskel, S.; Hoffmann, M. J. High capacity vertical aligned carbon nanotube/sulfur composite cathodes for lithium−sulfur batteries. *Chem. Commun.* **2012**, *48* (34), 4097−4099.

(19) Lyu, Z.; Xu, D.; Yang, L.; Che, R.; Feng, R.; Zhao, J.; Li, Y.; Wu, Q.; Wang, X.; Hu, Z. Hierarchical carbon nanocages confining high-loading sulfur for high-rate lithium-sulfur batteries. *Nano Energy* **2015**, *12*, 657−665.

(20) Zhang, J.; Yang, C.-P.; Yin, Y.-X.; Wan, L.-J.; Guo, Y.-G. Sulfur Encapsulated in Graphitic Carbon Nanocages for High-Rate and Long-Cycle Lithium-Sulfur Batteries. *Adv. Mater.* **2016**, *28* (43), 9539−9544.

(21) Ma, C.; Zheng, Z.; Jia, X.; Liu, X.; Wang, J.; Qiao, W.; Ling, L. Promoting the synergistic effect of sulfur immobilization and polysulfides trapping by nitrogen functionalized interconnected hollow carbon nanocages for high-performance lithium-sulfur batteries. *J. Power Sources* **2021**, *486*, 229358.
(22) Zhou, G.; Tian, H.; Jin, Y.; Tao, X.; Liu, B.; Zhang, R.; Seh, Z. W.; Zhuo, D.; Liu, Y.; Sun, J.; Zhao, J.; Zu, C.; Wu, D. S.; Zhang, Q.; Cui, Y. Catalytic oxidation of Li_2S on the surface of metal sulfides for Li-S batteries. *Proc. Natl. Acad. Sci. U. S. A.* **2017**, *114* (5), 840−845.
(23) Liu, X.; Huang, J. Q.; Zhang, Q.; Mai, L. Nanostructured Metal Oxides and Sulfides for Lithium-Sulfur Batteries. *Adv. Mater.* **2017**, *29* (20), 1601759.
(24) Liu, D.; Zhang, C.; Zhou, G.; Lv, W.; Ling, G.; Zhi, L.; Yang, Q. H. Catalytic Effects in Lithium-Sulfur Batteries: Promoted Sulfur Transformation and Reduced Shuttle Effect. *Advanced Science* **2018**, *5* (1), 1700270.
(25) Mei, S.; Jafta, C. J.; Lauermann, I.; Ran, Q.; Kärgell, M.; Ballauff, M.; Lu, Y. Porous Ti_4O_7 Particles with Interconnected-Pore Structure as a High-Efficiency Polysulfide Mediator for Lithium−Sulfur Batteries. *Adv. Funct. Mater.* **2017**, *27* (26), 1701176.
(26) Liang, X.; Kwok, C. Y.; Lodi-Marzano, F.; Pang, Q.; Cuisinier, M.; Huang, H.; Hart, C. J.; Houtarde, D.; Kaup, K.; Sommer, H.; Brezesinski, T.; Janek, J.; Nazar, L. F. Tuning Transition Metal Oxide-Sulfur Interactions for Long Life Lithium-Sulfur Batteries: The "Goldilocks" Principle. *Adv. Energy Mater.* **2016**, *6* (6), 1501636.
(27) Tao, X.; Wang, J.; Liu, C.; Wang, H.; Yao, H.; Zheng, G.; Seh, Z. W.; Cai, Q.; Li, W.; Zhou, G.; Zu, C.; Cui, Y. Balancing surface adsorption and diffusion of lithium-polysulfides on nonconductive oxides for lithium-sulfur battery design. *Nat. Commun.* **2016**, *7* (1), 11203.
(28) Zhao, M.; Peng, H.-J.; Zhang, Z.-W.; Li, B.-Q.; Chen, X.; Xie, J.; Chen, X.; Wei, J.-Y.; Zhang, Q.; Huang, J.-Q. Activating Inert Metallic Compounds for High-Rate Lithium-Sulfur Batteries Through In Situ Etching of Extrinsic Metal. *Angew. Chem., Int. Ed.* **2019**, *58* (12), 3779−3783.
(29) Sun, Z.; Zhang, J.; Yin, L.; Hu, G.; Fang, R.; Cheng, H.-M.; Li, F. Conductive porous vanadium nitride/graphene composite as chemical anchor of polysulfides for lithium-sulfur batteries. *Nat. Commun.* **2017**, *8* (1), 14627.
(30) Zhou, F.; Li, Z.; Luo, X.; Wu, T.; Jiang, B.; Lu, L.-L.; Yao, H.-B.; Antonietti, M.; Yu, S.-H. Low Cost Metal Carbide Nanocrystals as Binding and Electrocatalytic Sites for High Performance Li-S Batteries. *Nano Lett.* **2018**, *18* (2), 1035−1043.
(31) Yuan, H.; Chen, X.; Zhou, G.; Zhang, W.; Luo, J.; Huang, H.; Gan, Y.; Liang, C.; Xia, Y.; Zhang, J.; Wang, J.; Tao, X. Efficient Activation of Li_2S by Transition Metal Phosphides Nanoparticles for Highly Stable Lithium−Sulfur Batteries. *ACS Energy Letters* **2017**, *2* (7), 1711−1719.
(32) Shen, J.; Xu, X.; Liu, J.; Liu, Z.; Li, F.; Hu, R.; Liu, J.; Hou, X.; Feng, Y.; Yu, Y.; Zhu, M. Mechanistic Understanding of Metal Phosphide Host for Sulfur Cathode in High-Energy-Density Lithium−Sulfur Batteries. *ACS Nano* **2019**, *13* (8), 8986−8996.
(33) Wang, M.; Fan, L.; Sun, X.; Guan, B.; Jiang, B.; Wu, X.; Tian, D.; Sun, K.; Qiu, Y.; Yin, X.; Zhang, Y.; Zhang, N. Nitrogen-Doped $CoSe_2$ as a Bifunctional Catalyst for High Areal Capacity and Lean Electrolyte of Li-S Battery. *ACS Energy Letters* **2020**, *5* (9), 3041−3050.
(34) Tian, W.; Xi, B.; Feng, Z.; Li, H.; Feng, J.; Xiong, S. Sulfiphilic Few-Layered $MoSe_2$ Nanoflakes Decorated rGO as a Highly Efficient Sulfur Host for Lithium-Sulfur Batteries. *Adv. Energy Mater.* **2019**, *9* (36), 1901896.
(35) Wang, H.; Li, J.; Li, K.; Lin, Y.; Chen, J.; Gao, L.; Nicolosi, V.; Xiao, X.; Lee, J.-M. Transition metal nitrides for electrochemical energy applications. *Chem. Soc. Rev.* **2021**, *50* (2), 1354−1390.
(36) Mosavati, N.; Salley, S. O.; Ng, K. Y. S. Characterization and electrochemical activities of nanostructured transition metal nitrides as cathode materials for lithium sulfur batteries. *J. Power Sources* **2017**, *340*, 210−216.
(37) Li, Z.; He, Q.; Xu, X.; Zhao, Y.; Liu, X.; Zhou, C.; Ai, D.; Xia, L.; Mai, L. A 3D Nitrogen-Doped Graphene/TiN Nanowires Composite as a Strong Polysulfide Anchor for Lithium-Sulfur Batteries with Enhanced Rate Performance and High Areal Capacity. *Adv. Mater.* **2018**, *30* (45), 1804089.
(38) Cui, Z.; Zu, C.; Zhou, W.; Manthiram, A.; Goodenough, J. B. Mesoporous Titanium Nitride-Enabled Highly Stable Lithium-Sulfur Batteries. *Adv. Mater.* **2016**, *28* (32), 6926−6931.
(39) Liu, R.; Liu, W.; Bu, Y.; Yang, W.; Wang, C.; Priest, C.; Liu, Z.; Wang, Y.; Chen, J.; Wang, Y.; Cheng, J.; Lin, X.; Feng, X.; Wu, G.; Ma, Y.; Huang, W. Conductive Porous Laminated Vanadium Nitride as Carbon-Free Hosts for High-Loading Sulfur Cathodes in Lithium-Sulfur Batteries. *ACS Nano* **2020**, *14* (12), 17308−17320.
(40) Zhong, Y.; Chao, D.; Deng, S.; Zhan, J.; Fang, R.; Xia, Y.; Wang, Y.; Wang, X.; Xia, X.; Tu, J. Confining Sulfur in Integrated Composite Scaffold with Highly Porous Carbon Fibers/Vanadium Nitride Arrays for High-Performance Lithium-Sulfur Batteries. *Adv. Funct. Mater.* **2018**, *28* (38), 1706391.
(41) Zhang, L.; Chen, X.; Wan, F.; Niu, Z.; Wang, Y.; Zhang, Q.; Chen, J. Enhanced Electrochemical Kinetics and Polysulfide Traps of Indium Nitride for Highly Stable Lithium-Sulfur Batteries. *ACS Nano* **2018**, *12* (9), 9578−9586.
(42) Sun, Z.; Vijay, S.; Heenen, H. H.; Eng, A. Y. S.; Tu, W.; Zhao, Y.; Koh, S. W.; Gao, P.; Seh, Z. W.; Chan, K.; Li, H. Catalytic Polysulfide Conversion and Physiochemical Confinement for Lithium-Sulfur Batteries. *Adv. Energy Mater.* **2020**, *10* (22), 1904010.
(43) Deng, D.-R.; Xue, F.; Jia, Y.-J.; Ye, J.-C.; Bai, C.-D.; Zheng, M.-S.; Dong, Q.-F. Co4N Nanosheet Assembled Mesoporous Sphere as a Matrix for Ultrahigh Sulfur Content Lithium−Sulfur Batteries. *ACS Nano* **2017**, *11* (6), 6031−6039.
(44) Xiao, K.; Wang, J.; Chen, Z.; Qian, Y.; Liu, Z.; Zhang, L.; Chen, X.; Liu, J.; Fan, X.; Shen, Z. X. Improving Polysulfides Adsorption and Redox Kinetics by the Co_4N Nanoparticle/N-Doped Carbon Composites for Lithium-Sulfur Batteries. *Small* **2019**, *15* (25), 1901454.
(45) Li, R.; Peng, H.; Wu, Q.; Zhou, X.; He, J.; Shen, H.; Yang, M.; Li, C. Sandwich-like Catalyst-Carbon-Catalyst Trilayer Structure as a Compact 2D Host for Highly Stable Lithium-Sulfur Batteries. *Angew. Chem., Int. Ed.* **2020**, *59* (29), 12129−12138.
(46) Yang, J.-L.; Cai, D.-Q.; Hao, X.-G.; Huang, L.; Lin, Q.; Zeng, X.-T.; Zhao, S.-X.; Lv, W. Rich Heterointerfaces Enabling Rapid Polysulfides Conversion and Regulated Li_2S Deposition for High-Performance Lithium−Sulfur Batteries. *ACS Nano* **2021**, *15* (7), 11491−11500.
(47) Liu, H.; Shen, H.; Li, R.; Liu, S.; Turak, A.; Yang, M. Tungsten-Nitride-Coated Carbon Nanospheres as a Sulfur Host for High-Performance Lithium-Sulfur Batteries. *ChemElectroChem.* **2019**, *6* (7), 2074−2079.
(48) Sun, W.; Liu, C.; Li, Y.; Luo, S.; Liu, S.; Hong, X.; Xie, K.; Liu, Y.; Tan, X.; Zheng, C. Rational Construction of Fe_2N@C Yolk-Shell Nanoboxes as Multifunctional Hosts for Ultralong Lithium-Sulfur Batteries. *ACS Nano* **2019**, *13* (10), 12137−12147.
(49) Zhang, M.; Wang, L.; Wang, B.; Zhang, B.; Sun, X.; Wang, D.; Kong, Z.; Xu, L. Phosphorus-modified Fe_4N@N,P co-doped graphene as an efficient sulfur host for high-performance lithium-sulfur batteries. *Journal of Materials Chemistry A* **2021**, *9* (10), 6538−6546.
(50) Xu, F.; Ding, B.; Qiu, Y.; Dong, R.; Zhuang, W.; Xu, X.; Han, H.; Yang, J.; Wei, B.; Wang, H.; Kaskel, S. Generalized Domino-Driven Synthesis of Hollow Hybrid Carbon Spheres with Ultrafine Metal Nitrides/Oxides. *Matter* **2020**, *3* (1), 246−260.
(51) Yuan, H.; Peng, H.-J.; Li, B.-Q.; Xie, J.; Kong, L.; Zhao, M.; Chen, X.; Huang, J.-Q.; Zhang, Q. Conductive and Catalytic Triple-Phase Interfaces Enabling Uniform Nucleation in High-Rate Lithium−Sulfur Batteries. *Adv. Energy Mater.* **2019**, *9* (1), 1802768.
(52) Boyjoo, Y.; Shi, H.; Olsson, E.; Cai, Q.; Wu, Z.-S.; Liu, J.; Lu, G. Q. Molecular-Level Design of Pyrrhotite Electrocatalyst Decorated Hierarchical Porous Carbon Spheres as Nanoreactors for Lithium-Sulfur Batteries. *Adv. Energy Mater.* **2020**, *10* (20), 2000651.

https://doi.org/10.1021/acsnano.2c01992
ACS Nano 2022, 16, 10554−10565

(53) Wang, H.; Shao, Y.; Mei, S.; Lu, Y.; Zhang, M.; Sun, J.-k.; Matyjaszewski, K.; Antonietti, M.; Yuan, J. Polymer-Derived Heteroatom-Doped Porous Carbon Materials. *Chem. Rev.* **2020**, *120* (17), 9363−9419.
(54) Pan, H.; Cheng, Z.; Xiao, Z.; Li, X.; Wang, R. The Fusion of Imidazolium-Based Ionic Polymer and Carbon Nanotubes: One Type of New Heteroatom-Doped Carbon Precursors for High-Performance Lithium-Sulfur Batteries. *Adv. Funct. Mater.* **2017**, *27* (44), 1703936.
(55) Cheng, Z.; Pan, H.; Chen, J.; Meng, X.; Wang, R. Separator Modified by Cobalt-Embedded Carbon Nanosheets Enabling Chemisorption and Catalytic Effects of Polysulfides for High-Energy-Density Lithium-Sulfur Batteries. *Adv. Energy Mater.* **2019**, *9* (32), 1901609.
(56) Wang, H.; Min, S.; Wang, Q.; Li, D.; Casillas, G.; Ma, C.; Li, Y.; Liu, Z.; Li, L.-J.; Yuan, J.; Antonietti, M.; Wu, T. Nitrogen-Doped Nanoporous Carbon Membranes with Co/CoP Janus-Type Nanocrystals as Hydrogen Evolution Electrode in Both Acidic and Alkaline Environments. *ACS Nano* **2017**, *11* (4), 4358−4364.
(57) Balach, J.; Wu, H.; Polzer, F.; Kirmse, H.; Zhao, Q.; Wei, Z.; Yuan, J. Poly(ionic liquid)-derived nitrogen-doped hollow carbon spheres: synthesis and loading with Fe_2O3 for high-performance lithium ion batteries. *RSC Adv.* **2013**, *3* (21), 7979−7986.
(58) Soll, S.; Fellinger, T.-P.; Wang, X.; Zhao, Q.; Antonietti, M.; Yuan, J. Water Dispersible, Highly Graphitic and Nitrogen-Doped Carbon Nanobubbles. *Small* **2013**, *9* (24), 4135−4141.
(59) Li, Z.; Xiao, Z.; Li, P.; Meng, X.; Wang, R. Enhanced Chemisorption and Catalytic Effects toward Polysulfides by Modulating Hollow Nanoarchitectures for Long-Life Lithium−Sulfur Batteries. *Small* **2020**, *16* (4), 1906114.
(60) Zhang, W.; Kochovski, Z.; Lu, Y.; Schmidt, B. V. K. J.; Antonietti, M.; Yuan, J. Internal Morphology-Controllable Self-Assembly in Poly(Ionic Liquid) Nanoparticles. *ACS Nano* **2016**, *10* (8), 7731−7737.
(61) Fei, R.; Wang, H.; Wang, Q.; Qiu, R.; Tang, S.; Wang, R.; He, B.; Gong, Y.; Fan, H. J. In Situ Hard-Template Synthesis of Hollow Bowl-Like Carbon: A Potential Versatile Platform for Sodium and Zinc Ion Capacitors. *Adv. Energy Mater.* **2020**, *10* (47), 2002741.
(62) Gao, J.; Li, Y.; Peng, B.; Wang, G.; Zhang, G. The general construction of asymmetric bowl-like hollow nanostructures by grafting carbon-sheathed ultrasmall iron-based compounds onto carbon surfaces for use as superior anodes for sodium-ion hybrid capacitors. *Journal of Materials Chemistry A* **2019**, *7* (42), 24199−24204.
(63) Einert, M.; Wessel, C.; Badaczewski, F.; Leichtweiß, T.; Eufinger, C.; Janek, J.; Yuan, J.; Antonietti, M.; Smarsly, B. M. Nitrogen-Doped Carbon Electrodes: Influence of Microstructure and Nitrogen Configuration on the Electrical Conductivity of Carbonized Polyacrylonitrile and Poly(ionic liquid) Blends. *Macromol. Chem. Phys.* **2015**, *216* (19), 1930−1944.
(64) Leineweber, A.; Jacobs, H.; Hüning, F.; Lueken, H.; Kockelmann, W. Nitrogen ordering and ferromagnetic properties of ϵ-Fe_3N_{1+x} ($0.10 \leq x \leq 0.39$) and ϵ-$Fe_3(N_{0.80}C_{0.20})_{1.38}$. *J. Alloys Compd.* **2001**, *316* (1), 21−38.
(65) Chen, X.; Zeng, S.; Muheiyati, H.; Zhai, Y.; Li, C.; Ding, X.; Wang, L.; Wang, D.; Xu, L.; He, Y.; Qian, Y. Double-Shelled Ni-Fe-P/N-Doped Carbon Nanobox Derived from a Prussian Blue Analogue as an Electrode Material for K-Ion Batteries and Li-S Batteries. *ACS Energy Letters* **2019**, *4* (7), 1496−1504.
(66) Song, J.; Xu, T.; Gordin, M. L.; Zhu, P.; Lv, D.; Jiang, Y.-B.; Chen, Y.; Duan, Y.; Wang, D. Nitrogen-Doped Mesoporous Carbon Promoted Chemical Adsorption of Sulfur and Fabrication of High-Areal-Capacity Sulfur Cathode with Exceptional Cycling Stability for Lithium-Sulfur Batteries. *Adv. Funct. Mater.* **2014**, *24* (9), 1243−1250.
(67) Xie, J.; Li, B.-Q.; Peng, H.-J.; Song, Y.-W.; Zhao, M.; Chen, X.; Zhang, Q.; Huang, J.-Q. Implanting Atomic Cobalt within Mesoporous Carbon toward Highly Stable Lithium-Sulfur Batteries. *Adv. Mater.* **2019**, *31* (43), 1903813.
(68) Cheng, Q.; Mao, K.; Ma, L.; Yang, L.; Zou, L.; Zou, Z.; Hu, Z.; Yang, H. Encapsulation of Iron Nitride by Fe-N-C Shell Enabling Highly Efficient Electroreduction of CO_2 to CO. *ACS Energy Letters* **2018**, *3* (5), 1205−1211.
(69) Xiao, J.; Xu, Y.; Xia, Y.; Xi, J.; Wang, S. Ultra-small Fe_2N nanocrystals embedded into mesoporous nitrogen-doped graphitic carbon spheres as a highly active, stable, and methanol-tolerant electrocatalyst for the oxygen reduction reaction. *Nano Energy* **2016**, *24*, 121−129.
(70) Xi, Y.; Ye, X.; Duan, S.; Li, T.; Zhang, J.; Jia, L.; Yang, J.; Wang, J.; Liu, H.; Xiao, Q. Iron vacancies and surface modulation of iron disulfide nanoflowers as a high power/energy density cathode for ultralong-life stable Li storage. *Journal of Materials Chemistry A* **2020**, *8* (29), 14769−14777.
(71) He, J.; Bhargav, A.; Manthiram, A. High-Energy-Density, Long-Life Lithium-Sulfur Batteries with Practically Necessary Parameters Enabled by Low-Cost Fe-Ni Nanoalloy Catalysts. *ACS Nano* **2021**, *15* (5), 8583−8591.
(72) Peng, H.-J.; Zhang, Z.-W.; Huang, J.-Q.; Zhang, G.; Xie, J.; Xu, W.-T.; Shi, J.-L.; Chen, X.; Cheng, X.-B.; Zhang, Q. A Cooperative Interface for Highly Efficient Lithium-Sulfur Batteries. *Adv. Mater.* **2016**, *28* (43), 9551−9558.
(73) Zeng, P.; Liu, C.; Zhao, X.; Yuan, C.; Chen, Y.; Lin, H.; Zhang, L. Enhanced Catalytic Conversion of Polysulfides Using Bimetallic Co_7Fe_3 for High-Performance Lithium-Sulfur Batteries. *ACS Nano* **2020**, *14* (9), 11558−11569.
(74) Fan, F. Y.; Carter, W. C.; Chiang, Y.-M. Mechanism and Kinetics of Li_2S Precipitation in Lithium-Sulfur Batteries. *Adv. Mater.* **2015**, *27* (35), 5203−5209.
(75) Sun, J.-K.; Kochovski, Z.; Zhang, W.-Y.; Kirmse, H.; Lu, Y.; Antonietti, M.; Yuan, J. General Synthetic Route toward Highly Dispersed Metal Clusters Enabled by Poly(ionic liquid)s. *J. Am. Chem. Soc.* **2017**, *139* (26), 8971−8976.

https://doi.org/10.1021/acsnano.2c01992
ACS Nano 2022, 16, 10554−10565